Supplement of Atmos. Chem. Phys., 15, 2367–2386, 2015
http://www.atmos-chem-phys.net/15/2367/2015/
doi:10.5194/acp-15-2367-2015-supplement

Atmospheric Chemistry and Physics
Open Access

Supplement of

Kerb and urban increment of highly time-resolved trace elements in PM_{10}, $PM_{2.5}$ and $PM_{1.0}$ winter aerosol in London during ClearfLo 2012

S. Visser et al.

Correspondence to: M. Furger (markus.furger@psi.ch)

Supplement A: RDI backup filter and $PM_{1.0}$ cut off analysis

RDI backup filter analysis

RDI backup filters (Balston 050-11-BQ 2 µm, microfiber, fluorocarbon resin binder) from the ClearfLo winter campaign were immersed in water and sonicated for about 1.5 h. One filter per measurement site was available. Total sulphate (SO_4^{2-}) mass was obtained by analysing the solutions with ion chromatography and converted to concentrations by dividing by the total air volume that passed through the filter during the campaign.

Table S1 compares the S concentrations from the RDI $PM_{1.0-0.3}$ stage with S (from SO_4^{2-}) collected by the backup filter. The sum of both (Total S < 1 µm) is compared with S from AMS sulphate measurements. The ratios of 0.67 to 1.26 in the last column reveal reasonable mass-closure between the RDI and AMS.

Table S1. Comparison between S from RDI $PM_{1.0-0.3}$ fractions and backup filters (S from SO_4^{2-}) with S from the AMS (S from SO_4^{2-}). Units in ng m^{-3}. The ratio of S in the RDI to the AMS is given in the last column (ratio of RDI Total S < 1 µm to AMS S).

Site	RDI $PM_{1.0-0.3}$ S	S in backup filter	Total S <1 µm	AMS S	Ratio RDI : AMS
MR	127	398	525	607	**0.86**
NK	113	405	518	412	**1.26**
DE	145	359	504	749	**0.67**

RDI $PM_{1.0}$ cut off analysis

As noted in the main text and in Supplement C, elements whose mass is dominated by the $PM_{1.0}$ fraction are typically underestimated by RDI-SR-XRF relative to external measurements like the AMS and 24 h filter measurements. One explanation is that the collection efficiency of the RDI $PM_{1.0}$ stage is smaller than expected, e.g. by a larger-than-expected size cut off. We therefore performed new laboratory measurements of the RDI size-dependent collection efficiency, and compare these to earlier characterisations by Bukowiecki et al. (2009) and Richard et al. (2010).

Figure S1 shows the setup used for the collection efficiency measurements. $(NH_4)_2SO_4$, NH_4NO_3 and NaCl particles were nebulized, dried and size-selected using a differential mobility analyser (DMA, TSI, Inc., Shoreview, MN, USA), and then sampled with the RDI. The DMA was operated with sample and sheath flow rates of 0.3 and 3.0 L min^{-1}, respectively. A condensation particle counter (CPC1, TSI, Inc., Shoreview, MN, USA) with a flow rate of 1.0 L min^{-1} was continuously connected at the inlet stage of the RDI to measure the particles entering the RDI, and to correct for fluctuations in nebulizer performance. A second line led to an additional CPC (CPC2, 1 L min^{-1}) and an Aerodyne aerosol mass spectrometer (AMS, Aerodyne Research, Inc., Billerica, MA, USA) with a flow rate of 0.1 L min^{-1}. This line could be connected at the inlet, after the $PM_{2.5-1.0}$ (B) stage or after the $PM_{1.0-0.3}$ (C) stage. Measurements following the B and C stages were made by connecting the line to a small hole in the lid covering these stages, resulting in sampling of the air flow at a 90° angle (see picture in Figure S1). The total flow through the system was controlled by a mass flow controller connected to a clean air generator pumping air into the nebulizer and RDI simultaneously. The RDI was operated using three wheels with freshly mounted 6 µm polypropylene foils coated with Apiezon to minimize particle bouncing effects, to simulate ambient field measurements. Tests ruled out differences in measurements on the top or bottom side of the lid at the B and C stages. For the final results, all data was collected at the bottom side of the B and C stages.

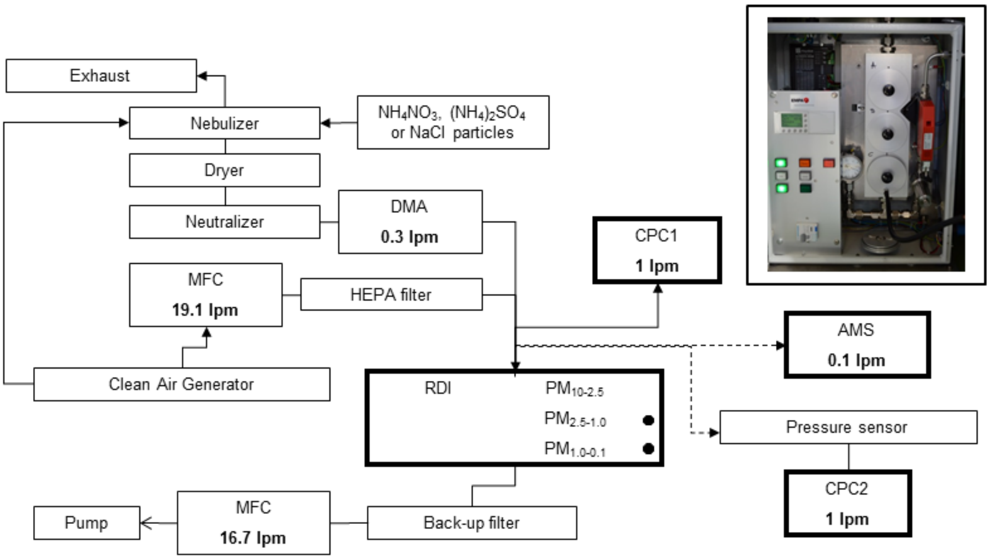

Figure S1. Setup of the collection efficiency measurements of the RDI $PM_{1.0}$ impactor stage. The line with the AMS and CPC2 was connected at the inlet, after the $PM_{2.5-1.0}$ or after the $PM_{1.0-0.3}$ stage. The picture of the RDI shows the connection at the bottom side of the lid of the $PM_{1.0-0.3}$ stage.

As noted above, measurements were conducted at the RDI inlet, after the B stage impactor (nominal size cut = 1.0 µm) and after the C stage impactor (nominal size cut = 0.1 µm). RDI collection efficiency at each stage is defined as 1 minus transmission. To correct for fluctuations in nebulizer concentrations, all data for a given set of CPC2/AMS measurements were normalized to a constant inlet (CPC1) concentration. Transmission from the inlet across the B stage impactor was between 90 and 100 % for all sizes (aerodynamic diameter *d* < 950 nm), indicating negligible particle losses and/or unintended collection of small particles. C stage collection efficiency (CE_C) was therefore calculated using Eq. (S1):

$$\boldsymbol{CE_C = 1 - \left(Conc_C * \frac{CPC1_{ref}}{CPC1_{measC}}\right) / \left(Conc_B * \frac{CPC1_{ref}}{CPC1_{measB}}\right)} \qquad \textbf{(S1)}$$

Concentrations were measured using both CPC2 and the AMS. For large particles, where the fraction of multiple charged particles passed by the DMA is negligible, these two methods yield similar results. For smaller particles, collection efficiency as calculated by the CPC2 is biased low due to the presence of multiple charged particles with larger diameters, as clearly evidenced from AMS size distributions. For simplicity, we therefore present only the AMS results here. RDI collection efficiencies are calculated by fitting a lognormal distribution to each mode and using the resulting mass concentrations in Eq. S1. This allows simultaneous calculation of RDI collection efficiencies for several sizes, providing an internal consistency and stability check for the measurements.

Figure S2 shows the collection efficiency of the $PM_{1.0\text{-}0.3}$ (C stage) nozzle for two RDIs (RDI1 and RDI2) as a function of *d* for NH_4NO_3 particles. *D* is calculated from AMS size measurements, assuming a density of 1.74 and a Jayne shape factor (DeCarlo et al., 2004) of 0.8. Cut points are estimated by a sigmoidal fit to the collection efficiency curves, and yield different cut points for the two RDIs. RDI1 has a cut point of 290 ± 25 nm and RDI2 a cut point of 410 ± 15 nm. This discrepancy was investigated using RDI2 equipped with the $PM_{1.0\text{-}0.3}$ nozzle of RDI1 (RDI2 (nozzle RDI1)), demonstrating that the difference between the two RDIs is governed by nozzle performance, because the cut point of this system is 300 ± 20 nm and therefore closer to the RDI1 performance. Similar cut points for the various systems were obtained using $(NH_4)_2SO_4$ and NaCl particles (not shown).

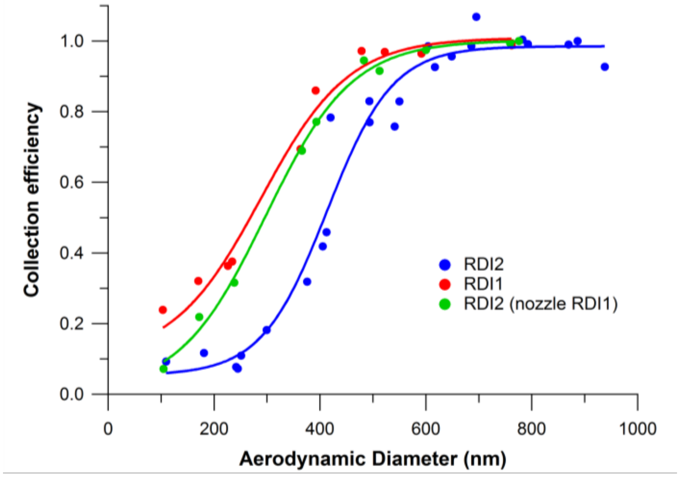

Figure S2. Collection efficiency of the RDI $PM_{1.0\text{-}0.3}$ impactor stage as a function of aerodynamic diameter.

Measurements of the nozzle sizes under a microscope reveal small differences between the RDIs. A 1.0 µm cut point at the B stage impactor is obtained with a nozzle size of 0.68 x 10 mm. The RDI1 and RDI2 B stage nozzles were 0.70 x 10 mm, and a third RDI that was used at Marylebone Road during ClearfLo had a size of 0.71 x 10 mm. The C stage nozzle size should measure 0.30 x 10 mm for a cut point of 0.1 µm. However, the nozzle sizes were 0.30-0.31 x 10, 0.30-0.32 x 10 and 0.32 x 10 for RDI1, RDI2 and the third RDI, respectively. We expect the deviations from these measurements from the machining of the nozzles, resulting in higher cut points than expected for the $PM_{1.0}$ stage, and possibly also for the $PM_{2.5\text{-}1.0}$ stage.

Conclusions

The $PM_{1.0\text{-}0.3}$ collection efficiency curves are different for the two RDIs. RDI2 has a larger small-end cut point of 410 ± 15 nm than RDI1 of 290 ± 25 nm. RDI2 with the $PM_{1.0\text{-}0.3}$ nozzle of RDI1 resulted in a similar cut point of RDI1 of 300 ± 20 nm. The slightly larger nozzles than theoretically calculated are the likely reason for the observed increase in the small-end cut point of the $PM_{1.0\text{-}0.3}$ nozzle and thus in reduced particle collection at the C stage.

Supplement B: Changes in SR-XRF analysis

The data described in the main text was obtained with RDI-SR-XRF analysis. The following significant changes were made in the SR-XRF analysis compared to the methodology described in Bukowiecki et al. (2005, 2008) and Richard et al. (2010):

1. At SLS, we replaced the silicon drift detector (Roentec Xflash 2001 type 1102, Bruker AXS) with an e2v SiriusSD detector (SiriusSD-30133LE-IS). This detector is equipped with a thin polymer window resulting in a wider energy range down to about 300 eV and a better energy resolution of 133 eV (Mn Kα at 5.9 keV). In addition, the setup accepts a higher throughput resulting in negligible dead time effects. We also replaced the helium chamber with an in-house built vacuum chamber (sample exposure system for micro-X-ray fluorescence measurements, SESmiX) which reaches about 10^{-6} bar. This extended the measured range of elements down to Na and Mg.

2. Reference standards for calibration of element fluorescence counts to mass concentrations were produced on the same 6 µm PP substrate as used for RDI sampling, in contrast to the previous standard where a much thicker 100 µm PET foil (Folex, BG-32.5 RS plus) was used. Two standards suitable for measurements at both SLS and HASYLAB contained elements in equal concentrations, and have a similar mix of elements as the standard previously used. Two additional standards containing only specifically selected light elements were produced. One standard contained Na, Al, P, Cl and Ca; the other Mg, Si, S, K and Ca. The concentrations of these elements were increased by a factor 3.8 relative to the other two standards to improve signal-to-noise ratios in the SR-XRF calibration. Co was added to these additional standards, but in the same concentration as in the other two foils and was used as a quality check of the fabrication procedure of the four standards. The concentration difference of the light elements was taken into account before applying the relative calibration of the sample elements. The new reference standards allowed the use of identical geometry and irradiation time for RDI samples and reference standards, meaning that all SR-XRF measurements exhibit the same scattering and secondary fluorescence excitation. This reduced uncertainties in both the absolute and relative calibration of the samples.

3. Previously, spectra were fitted with the WinAxil software package (Canberra Inc; Van Espen et al., 1986). This rather old spectral fitting package allows little flexibility in spectrum continuum correction and peak fitting. PyMCA (Sole et al., 2007) on the other hand, is more flexible, but lacks the possibility to save uncertainty calculations in batch mode. In this study, spectra were fitted with an in-house developed software package called Spectral Analysis for Multiple Instruments – toolkit for XRF (SAMI-XRF) using the IGOR Pro software environment (Wavemetrics, Inc., Portland, OR, USA) to evaluate the data and create custom interfaces to accomplish specialized tasks. SAMI sequentially determines (1) energy calibration of the X-ray line as a function of detector channel; (2) spectrum continuum correction; (3) peak width calibration as a function of energy (assuming Gaussian peak shape and a general square root law of the full-width-half-maximum (FWHM) energy relation); and (4) peak fitting of the entire spectrum, at which stage only peak heights are fitted as a free parameter and all other parameters are fixed. Steps (1) and (3) are performed with user-selected reference peaks, and incorporates fitting of complex (multi-Gaussian) peak shapes caused by nearly complete overlapping $K\alpha_1$ and $K\alpha_2$ lines. Step (2) utilizes collected spectra of a blank foil as a reference for the continuum shape, and scales this reference to user-selected element-free regions of the processed spectra. Step (4) allows lines to be fitted freely or fixed to another line, e.g.

to the strongest line in a shell. For example, the Kα_2 and Kβ lines can be fixed to the Kα_1 line according to the relative intensities given by Bearden (1967). In this study, all lines within an electron shell were fitted fixed to the strongest line in that shell. Additionally, Ni, Cu and Zn L$\alpha_{1,2}$ lines were fixed to the Kα_1 line to reduce the influence of peak overlap with Na. The ratios of L$\alpha_{1,2}$ to Kα_1 for Ni, Cu and Zn were determined by fitting calibration standards having these elements but low Na. Final fits were then obtained using the acquired relations, thereby reducing uncertainties in the Na concentrations due to peak overlap and improving Na quantification.

Supplement C: Data intercomparison

A short description of the data intercomparison between RDI-SR-XRF data and independent filter data is given in Sect. 3 of the main text. Here the details of this comparison are given. We compare XRF data with filter data (24 h PM_{10} trace element data analysed with ICP-MS; roughly 9 % uncertainty at a 95 % confidence interval and calibrated with NIST standards) for 18 elements collected at MR and NK (no filter data was available at DE). For this comparison, the three size ranges of the RDI were summed up to total PM_{10} and averaged to the filter collection period. The intercomparison results are shown in Fig. S3, and are divided into four groups to facilitate discussion. Fit coefficients and Pearson's *R* values for the intercomparison are shown in Table S2, while XRF uncertainties and detection limits are given in Table S3. For most elements the sample inhomogeneity provides the largest source of uncertainty of maximal 20 %. Significant uncertainties of 54-9 % in Na-Ca arise from corrections on self-absorption effects for the calibration standards. We assume a static size distribution of the coarse and intermediate fraction ambient samples. Therefore, no additional uncertainties arise from self-absorption corrections in the samples. RDI flow rate fluctuations are estimated at a maximum of 5 %. Absolute and relative calibration uncertainties are larger for lighter elements due to their low fluorescence yields, making them harder to detect. For Na-K these uncertainties are 13 %, for Ca-Pb only 2 %. The last source of uncertainty is the energy calibration of an X-ray line as function of detector channel and shows the effect of line overlap in the detection of a specific line. The uncertainties range between 1 and 22 % for most elements, but are around 60 % for Mn due to the overlap with Fe being present in much higher concentrations (on average a factor of 55). Overall, the total uncertainties are estimated at 21-40 % for most elements (46-83 % for Mn; 60-43 % for Na-Si). All RDI data points lie well above their detection limits (last column Table S3).

Elements shown in Fig. S3a (Al, Ca, Ti, Mn, Fe, Cu, Zn, Sr, Sb, Ba) agree within approximately ± 50 % with good correlations (Pearson's *R* > 0.78). Na and Mg are shown separately in Fig. S3b, because these elements are strongest affected by XRF self-absorption. In Fig. S3c-d, we show elements for which the intercomparison shows significant biases and/or no significant correlation between RDI and filters. Note that the elements exhibiting good agreement in Fig. 3a-b span orders of magnitude difference in concentration (and fluorescence counts), suggesting that there are no global or concentration-dependent biases in the RDI-SR-XRF data. For elements exhibiting lesser agreement (Fig. S3c-d), this leaves the element relative calibration (i.e. element fluorescence yield as a function of line energy), spectral peak fitting, and instrument size cut points as potential sources of error in the XRF analysis.

Figure S3b shows good agreement for Na and Mg within a factor of 1.10-1.30 and good correlations (Pearson's *R* 0.89-0.99) despite the large correction of the RDI data due to self-absorption effects in the calibration standards and the coarse and intermediate ambient samples. This leads to significant uncertainty in the absolute concentrations of those elements. Furthermore, the XRF relative calibration curve for Na and Mg is difficult to constrain due to the low response of these elements, but only led to an uncertainty of 13 % (for Na-K compared to 2 % for Ca-Pb).

Figure S3c shows good correlations for Mo (Pearson's *R* = 0.90), but the RDI measures a factor 2.4 higher concentrations than found on the filters, whereas Ni shows no significant correlation between RDI and filters (Pearson's *R* = 0.56). The most likely reason for the discrepancy between both methods is the ICP-MS extraction efficiency. This was 66 % for Ni, but unknown for Mo, leading to increased uncertainties in the absolute concentrations of the filter data. As shown in the main text, the RDI time series of these elements (including both urban/kerb increments and diurnal/weekly cycles) are consistent with those of elements expected to be co-emitted by the same sources. Visual inspection of the spectrum indicates that significant interferences between lines are unlikely, and this is confirmed by peak fitting sensitivity tests investigating the response of the calculated concentrations to uncertainties in line energy calibration (i.e. energy as a function of detector channel). We estimate a 3 % uncertainty in the measurement of Mo due to spectral analysis and an overall uncertainty of 21 %. Mo falls in a well-constrained region of the calibration curve (although is not directly measured on calibration foils), so relative calibration errors would require a systematic bias across this entire region of the calibration curve. While there are not enough jointly measured elements within the intercomparison to evaluate this possibility, good agreement between RDI and filter measurements is obtained through Sr (Kα = 14.1 keV) and at Sb (Kα = 26.4 keV) (Mo Kα lines fall at 17.5 keV), suggesting such a bias is unlikely. Spectral analysis uncertainties are 6 % for Ni (overall uncertainty of 22 %). Unlike Mo, the relative calibration is well-constrained both in terms of elements directly measured on calibration foils and in terms of intercomparison with nearby elements in the XRF calibration curve, where Ni falls just above Mn and Fe and just below Cu and Zn. RDI and filter measurements are shown to be in good agreement for these six elements in Fig. S3a.

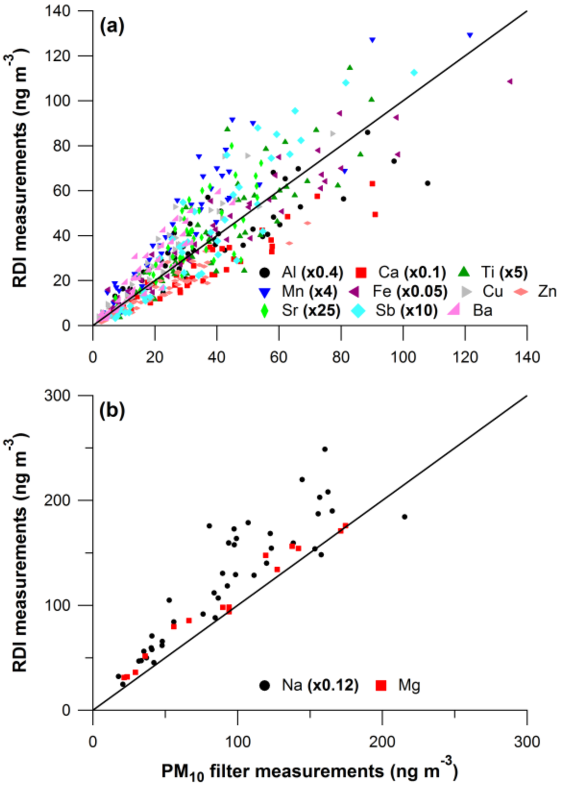

Figure S3. Total PM$_{10}$ element mass concentrations measured by the RDI (sum of PM$_{10\text{-}2.5}$, PM$_{2.5\text{-}1.0}$ and PM$_{1.0\text{-}0.3}$ fractions) at MR and NK averaged to 24 h versus 24 h PM$_{10}$ filter measurements of elements for (a) elements that agree within ± 50 %, (b) elements that agree but have a higher uncertainty due to self-absorption corrections, (c) elements with poor correlations, (d) other elements. The one-to-one line is added in black. See Table S2 for fit coefficients and Pearson's *R* values. Note that many elements are scaled to improve visualization.

Table S2. Fit coefficients and Pearson's *R* values for elements measured with the RDI ($PM_{10-2.5}$, $PM_{2.5-1.0}$ and $PM_{1.0-0.3}$ fractions summed to total PM_{10} and averaged to 24 h) relative to 24 h PM_{10} filter measurements. Data points were fitted with an orthogonal fit and forced zero intercept.

Element	Fit coefficient	Pearson's *R*
Na	1.32	0.89
Mg	1.09	0.99
Al	0.90	0.88
K	0.46	0.78
Ca	0.70	0.94
Ti	1.04	0.86
V	0.17	0.66
Mn	1.37	0.91
Fe	0.95	0.96
Ni	0.71	0.56
Cu	1.30	0.95
Zn	0.70	0.94
Sr	1.21	0.78
Mo	2.35	0.90
Sn	0.43	0.98
Sb	1.18	0.93
Ba	1.36	0.94
Pb	0.34	0.61

The elements K, V, Sn and Pb in Fig. S3d show reasonable correlations between RDI and filter measurements (Pearson's *R* > 0.61) but the RDI data is less than half the filter data (filter measurements of K and Sn only at NK). Pb has a significant fraction of the mass in the fine fraction (see Fig. 2 in main text). Underestimation by the RDI is explained by its small-end cut point of 290-410 nm. Typically, K, V and Sn are also mainly emitted in the fine fraction, and might be affected by the cut off similarly to Pb.

S is a useful element for evaluation of the small-end cut off, as it is dominant in the fine fraction and measurable by several techniques. Therefore, we compared S data obtained with the RDI to simultaneous S mass calculated from sulphate (SO_4) measured by an AMS at MR, NK, and DE. The results in Supplement A show that the S mass in the RDI is on average about 4.5 times lower than that measured by the AMS. This is consistent with the difference between RDI and filter measurements for fine fraction dominated elements. The RDI backup filter, which collects particles too small to impact at the $PM_{1.0-0.3}$ stage, was analysed for SO_4^{2-} using ion chromatography (Supplement A). Adding the S from this analysis to the S collected at the RDI $PM_{1.0-0.3}$ stage yielded mass closure with the S from AMS measurements within ~ 30 % at all three sites. This suggests that elements with considerable mass in the small end of the $PM_{1.0}$ size range are not sampled by the $PM_{1.0-0.3}$ stage. This affects S and Pb, and potentially also K, S, Zn, Br and Sn. To further investigate this effect, new RDI collection efficiency measurements for the $PM_{1.0}$ deposition stage were performed (Supplement A). The actual small-end cut off was determined to be 290-410 nm, rather than the previously measured value of 100 nm (Bukowiecki et al., 2009; Richard et al., 2010), and found to be very sensitive to the machining tolerances of the $PM_{1.0}$ nozzle.

Only a small fraction of the measured elements are affected by this cut off issue in the sense that absolute values are smaller than with a $PM_{1.0-0.1}$ stage. Further, because the analyses presented in the main text depends on site-to-site ratios (for the same element) and relative concentration changes, potential biases are reduced by the similar (though not identical, see Fig. S2 in Supplement A) cut offs of the different RDI units. The conclusions presented in the main text are thus not significantly affected by this artefact.

Table S3. Estimated total uncertainty (% of measured value) of the calculated element concentrations per size fraction, and detection limits for each element (ng m^{-3}).

Element	PM$_{10-2.5}$ (%)[a]	PM$_{2.5-1.0}$ (%)[a]	PM$_{1.0-0.3}$ (%)[a]	DL (ng m^{-3})[b]
Na	59	59	60	2.552
Mg	55	55	55	0.962
Al	48	48	48	1.709
Si	43	43	43	0.420
P	37	37	37	0.118
S	34	34	34	0.503
Cl	31	31	31	0.158
K	28	28	28	0.031
Ca	23	23	23	0.267
Ti	24	26	27	0.024
V	30	30	24	0.008
Cr	27	27	26	0.015
Mn	83	69	46	0.042
Fe	21	21	21	0.033
Ni	22	22	21	0.005
Cu	21	21	21	0.028
Zn	21	21	21	0.058
Br	21	21	21	0.117
Sr	21	21	21	0.036
Zr	21	21	21	0.036
Mo	21	21	21	0.037
Sn	21	21	21	0.061
Sb	21	21	21	0.052
Ba	21	21	21	0.254
Pb	21	21	21	0.137

[a] Combination of uncertainties regarding sample inhomogeneity (20 %), self-absorption corrections (Na 54, Mg 49, Al 41, Si 35, P 27, S 23, Cl 19, K 13 and Ca 9 %)[d], RDI flow rate (5 %), absolute and relative calibration (Na-K 13 %, Ca-Pb 2 %) and spectral analysis specific per element and size fraction (median uncertainties for all data points).

[b] Taken as 3x the standard deviation of the spectra signals used for continuum corrections.

[c] Na uncertainties might be underestimated due to the overlap with the L lines of Ni, Cu and Zn. In the current analysis the ratio of the Lα to Kα lines are determined empirically, and quantification of the associated uncertainties is under investigation.

[d] Uncertainties regarding self-absorption corrections are based on the microscopic analysis of the particle size on the calibration standards. The particle size of the dried droplets shows a geometric mean of the volume size distribution of 9 µm, and 50 % of the particles are in the range 4-14 µm (see also Table 2 in main text).

Supplement D: Additional tables and figures

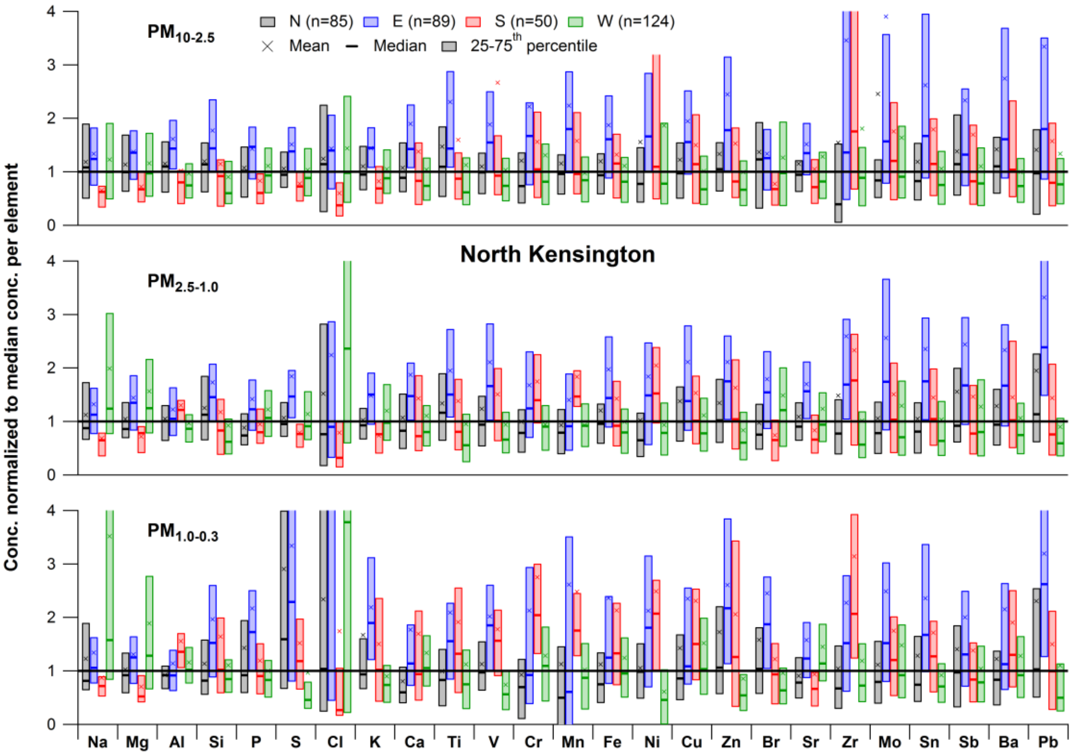

Figure S4. Same as Fig. 4 in main text, but for NK with mean, median and 25-75th percentile trace element concentrations split in four wind direction sectors (N, E, S, W) normalized to the global median concentration per element for $PM_{10-2.5}$ (top), $PM_{2.5-1.0}$ (middle) and $PM_{1.0-0.3}$ (bottom). See Sect. 4.2.2 for the definition of the wind direction sectors.

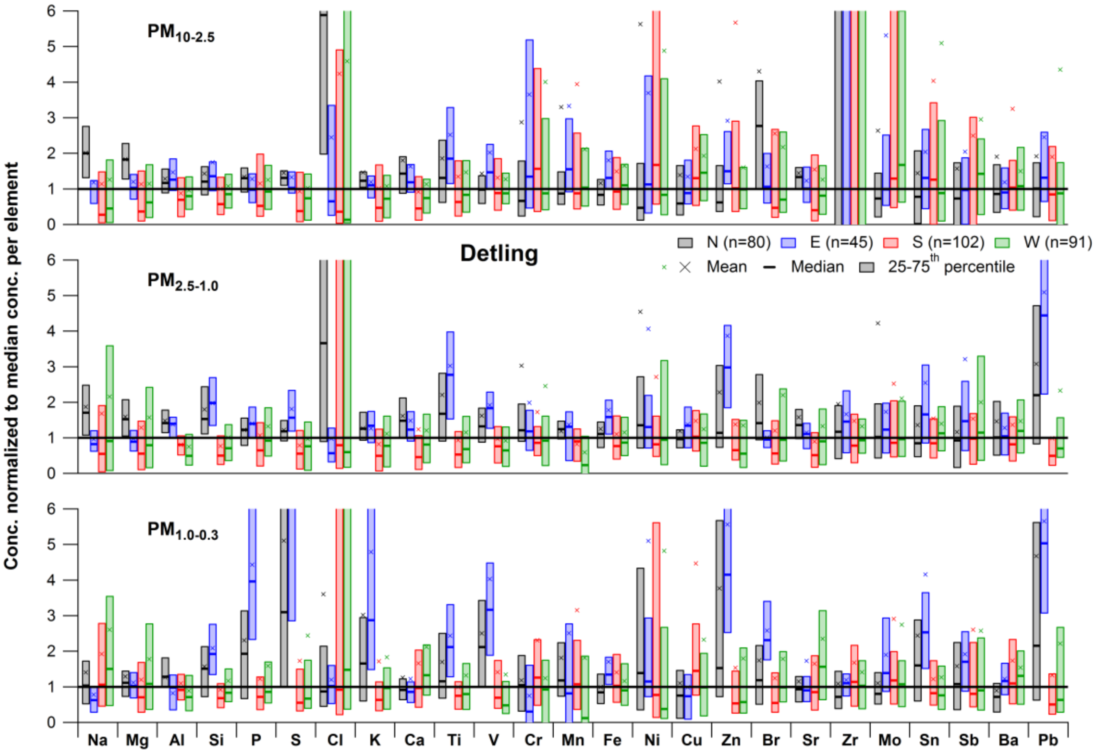

Figure S5. Same as Fig. 4, but for DE with mean, median and 25-75th percentile trace element concentrations split in four wind direction sectors (N, E, S, W) normalized to the global median concentration per element for $PM_{10-2.5}$ (top), $PM_{2.5-1.0}$ (middle) and $PM_{1.0-0.3}$ (bottom). See Sect. 4.2.2 for the definition of the wind direction sectors.

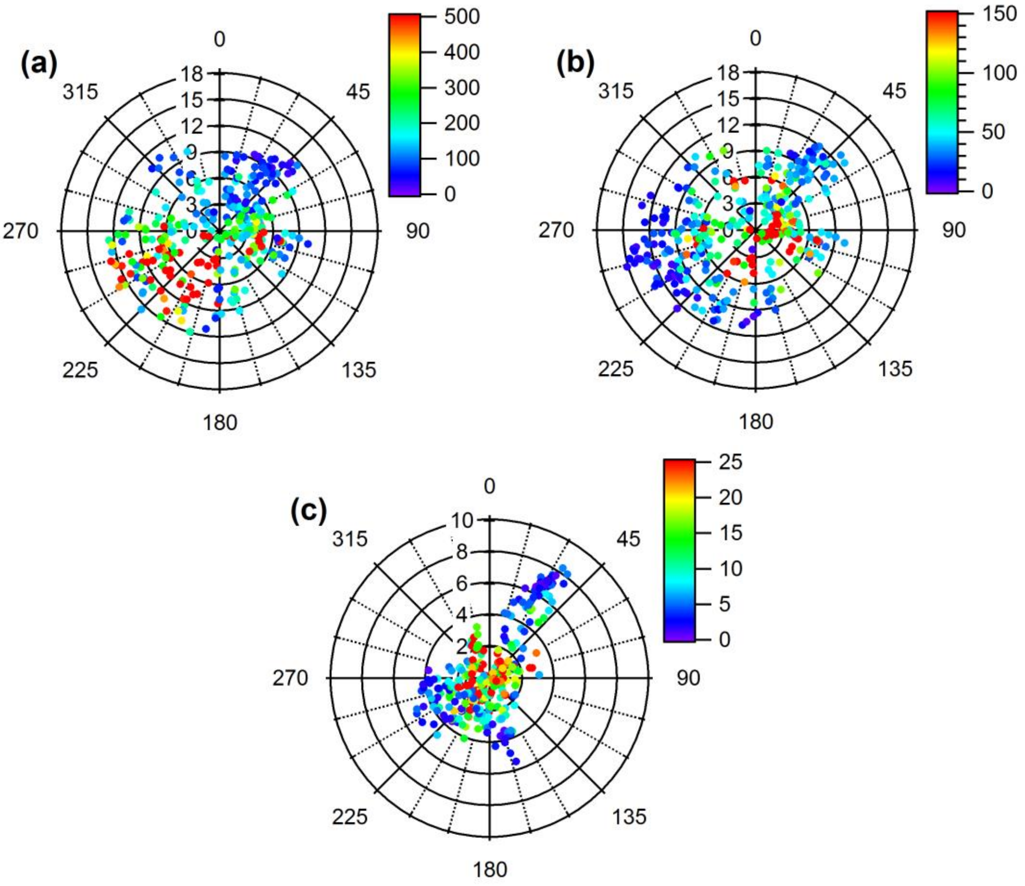

Figure S6. Wind roses as a function of wind direction (angle) and wind speed (diameter) at (a) BT Tower, color-coded by NO_x concentrations (ppb) at MR, (b) BT Tower, color-coded by NO_x concentrations (ppb) at NK, (c) DE, color-coded by NO_x concentrations (ppb) at DE for the RDI sampling periods (see Table 1 in main text).

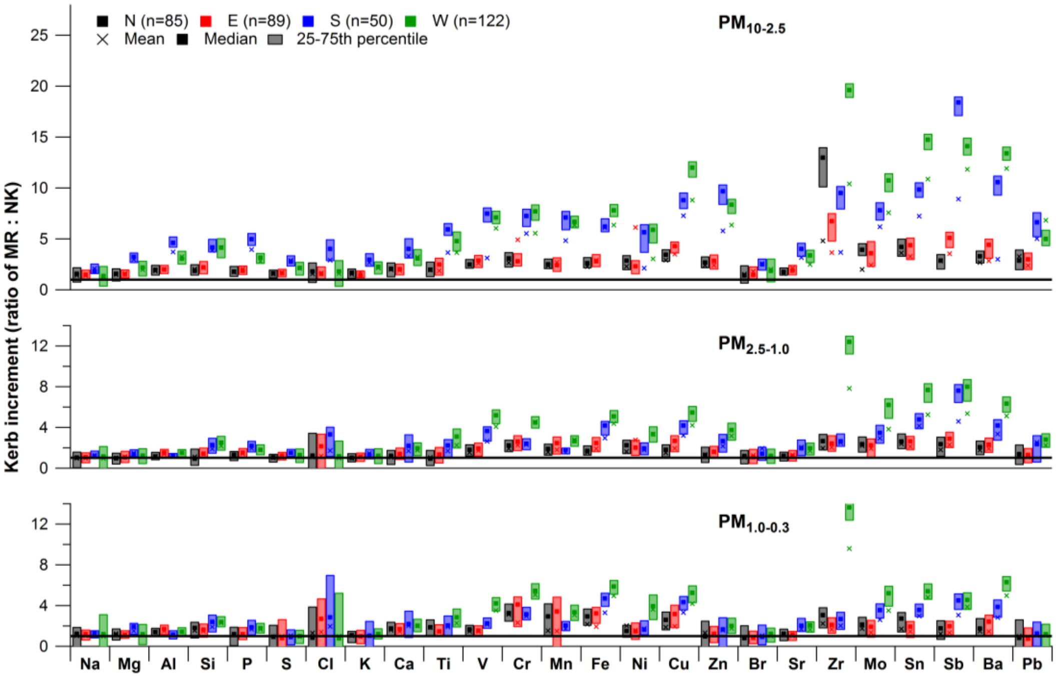

Figure S7. Same as Fig. 5, but with mean, median and 25-75th percentile kerb increment values for trace elements at MR relative to NK for $PM_{10-2.5}$ (top), $PM_{2.5-1.0}$ (middle) and $PM_{1.0-0.3}$ (bottom) split in N, E, S and W wind sectors. See Sect. 4.2.2 for the definition of the wind direction sectors.

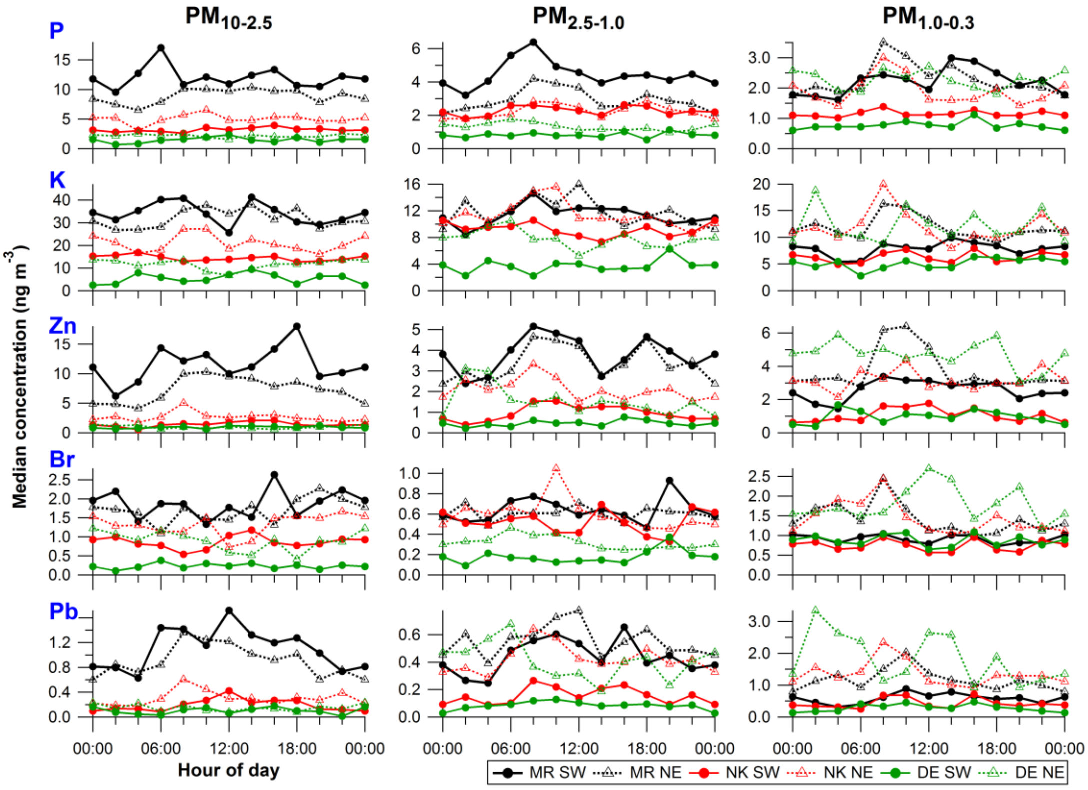

Figure S8. Same as Fig. 6, but for all other elements: P, K, Br, Zn, Pb (regional background); Mg (sea salt), Al, Ca, Ti, Sr (mineral dust); Cl (sea salt), V, Cr, Mn, Ni (traffic-related); Cu, Zr, Mo, Sn, Ba (brake wear). Diurnal cycles of 2 h median concentrations for $PM_{10-2.5}$ (left), $PM_{2.5-1.0}$ (middle) and $PM_{1.0-0.3}$ (right) at MR, NK, DE split in SW and NE wind sectors. See Sect. 4.2.2 for the definition of the wind direction sectors. Hour of day is start of 2 h sampling period, so 00:00 LT means sampling from 00:00 to 02:00 LT.

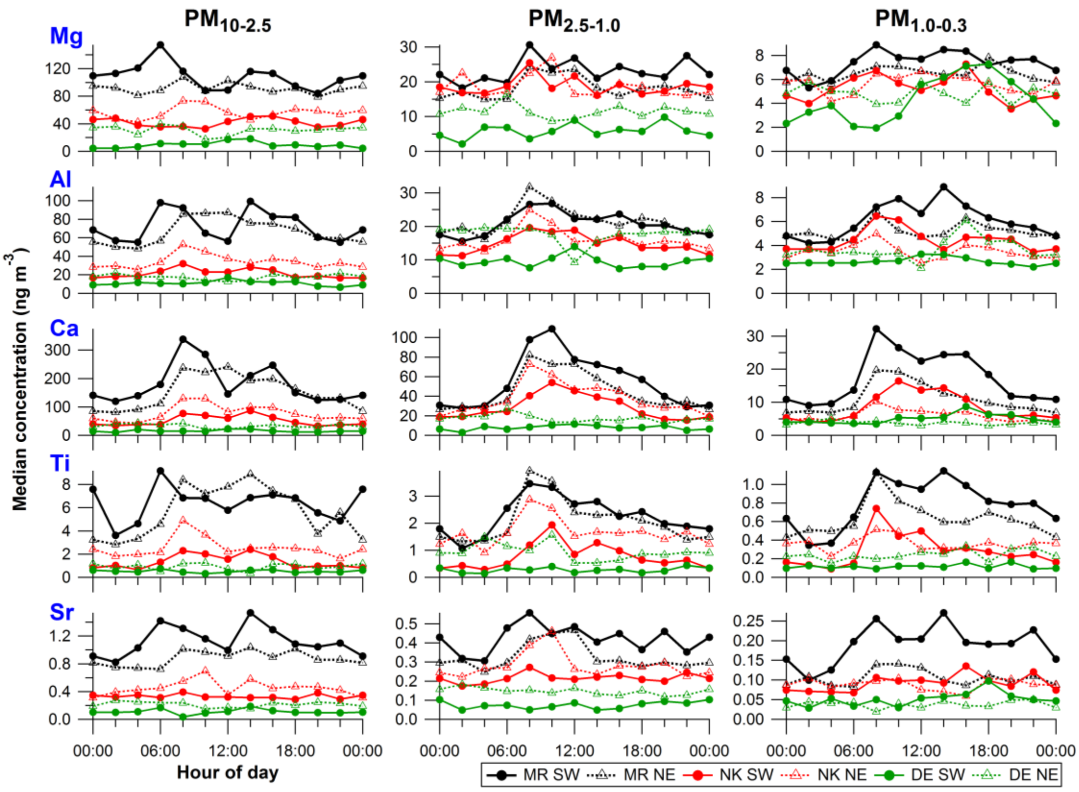

Figure S8. Continued.

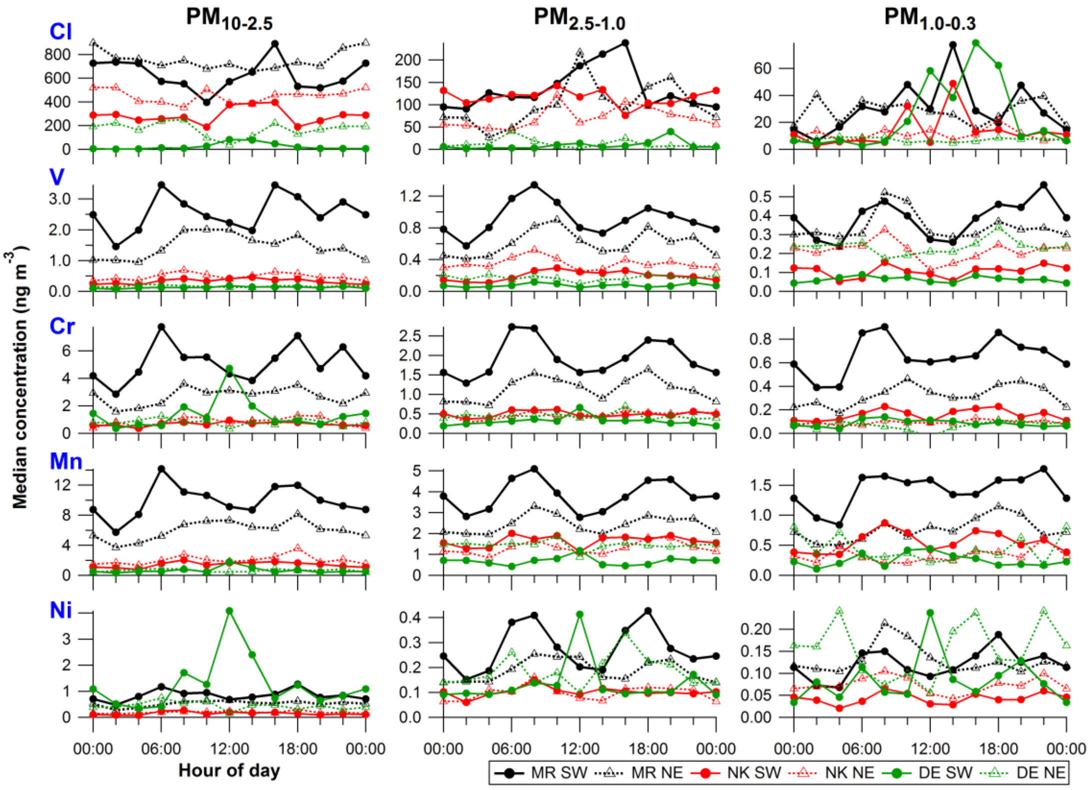

Figure S8. Continued.

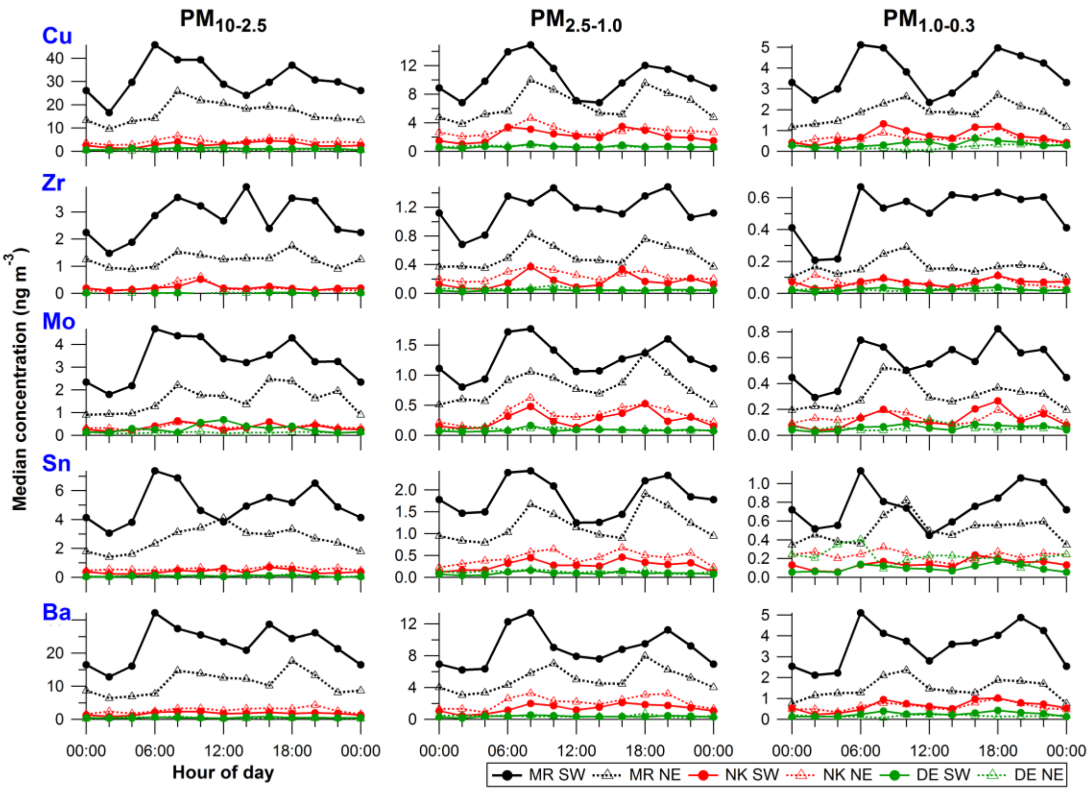

Figure S8. Continued.

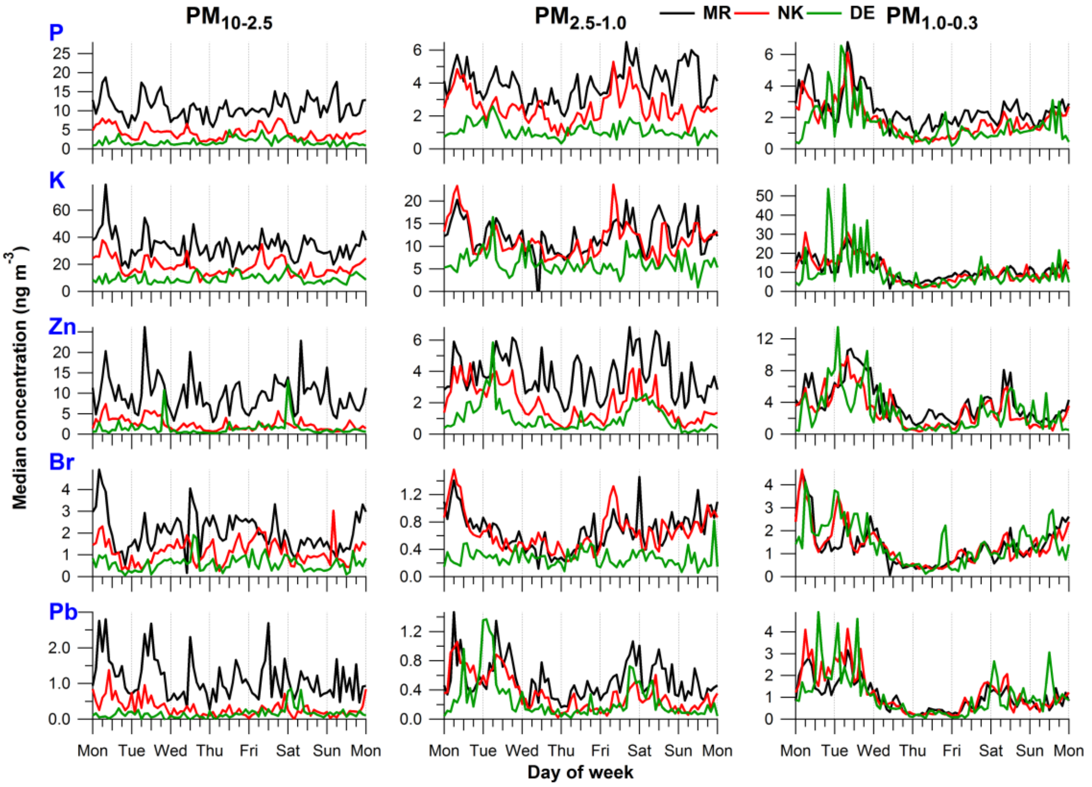

Figure S9. Same as Fig. 7, but for all other elements: P, K, Br, Zn, Pb (regional background); Mg (sea salt), Al, Ca, Ti, Sr (mineral dust); Cl (sea salt), V, Cr, Mn, Ni (traffic-related); Cu, Zr, Mo, Sn, Ba (brake wear). Weekly cycles of 2 h median concentrations for $PM_{10\text{-}2.5}$ (left), $PM_{2.5\text{-}1.0}$ (middle) and $PM_{1.0\text{-}0.3}$ (right) at MR, NK, DE.

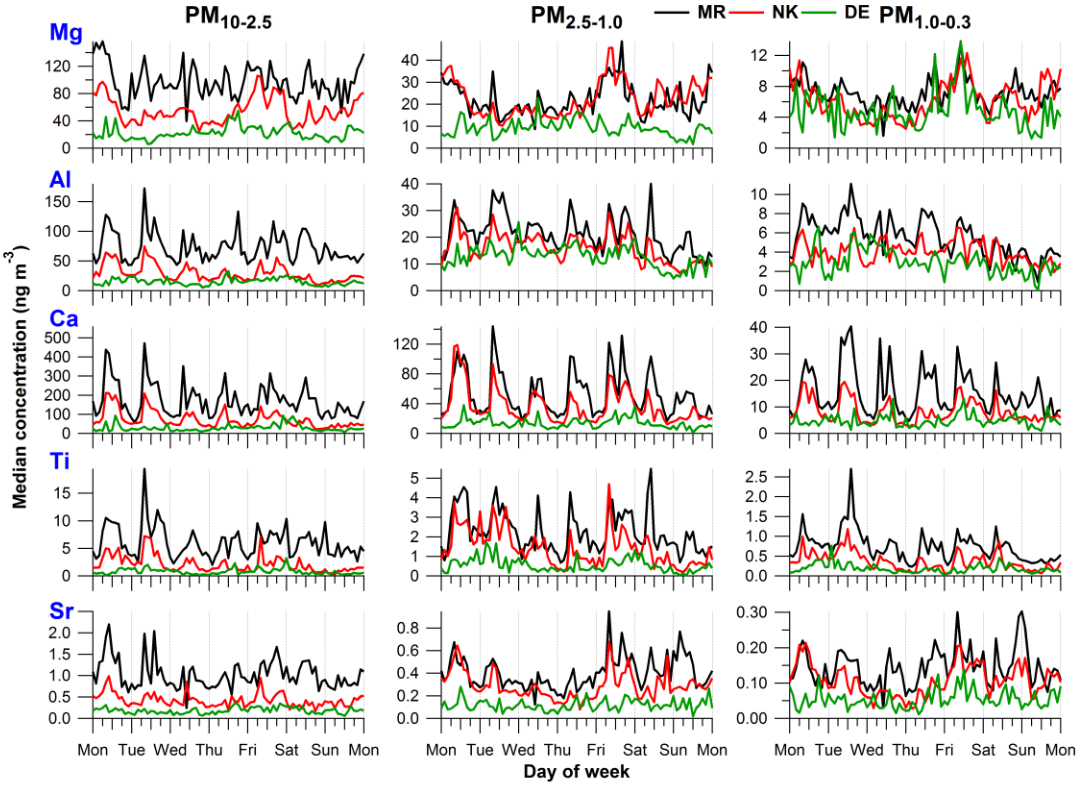

Figure S9. Continued.

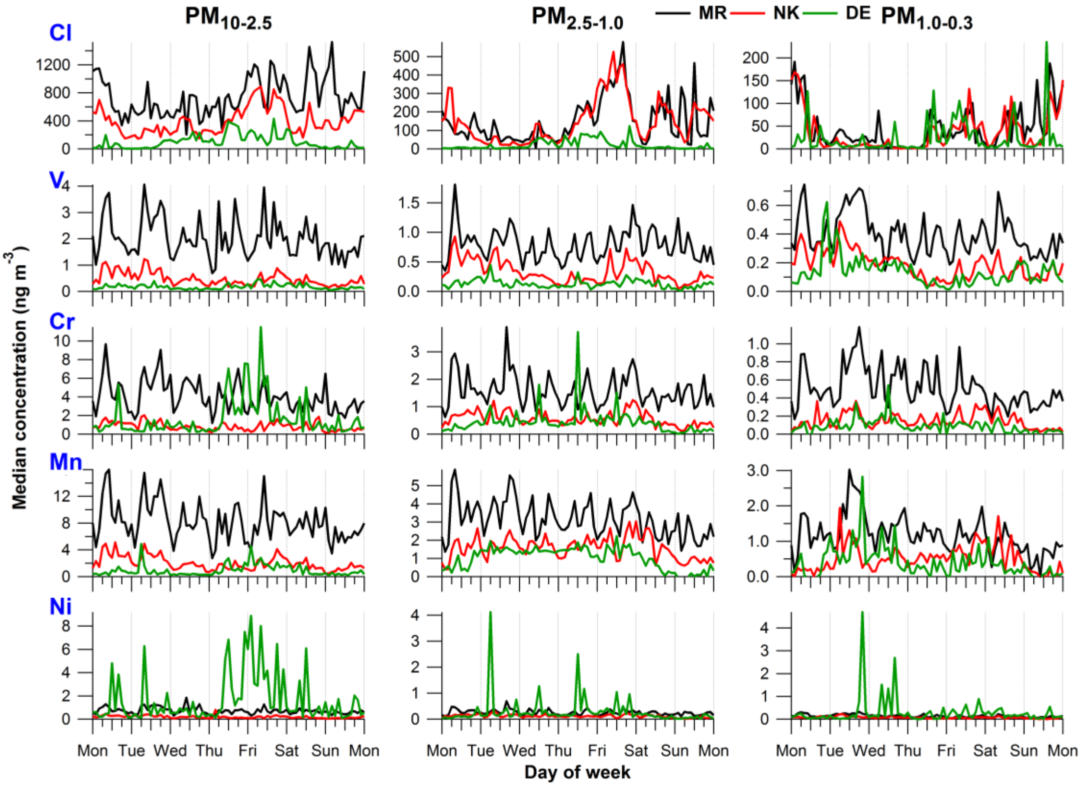

Figure S9. Continued.

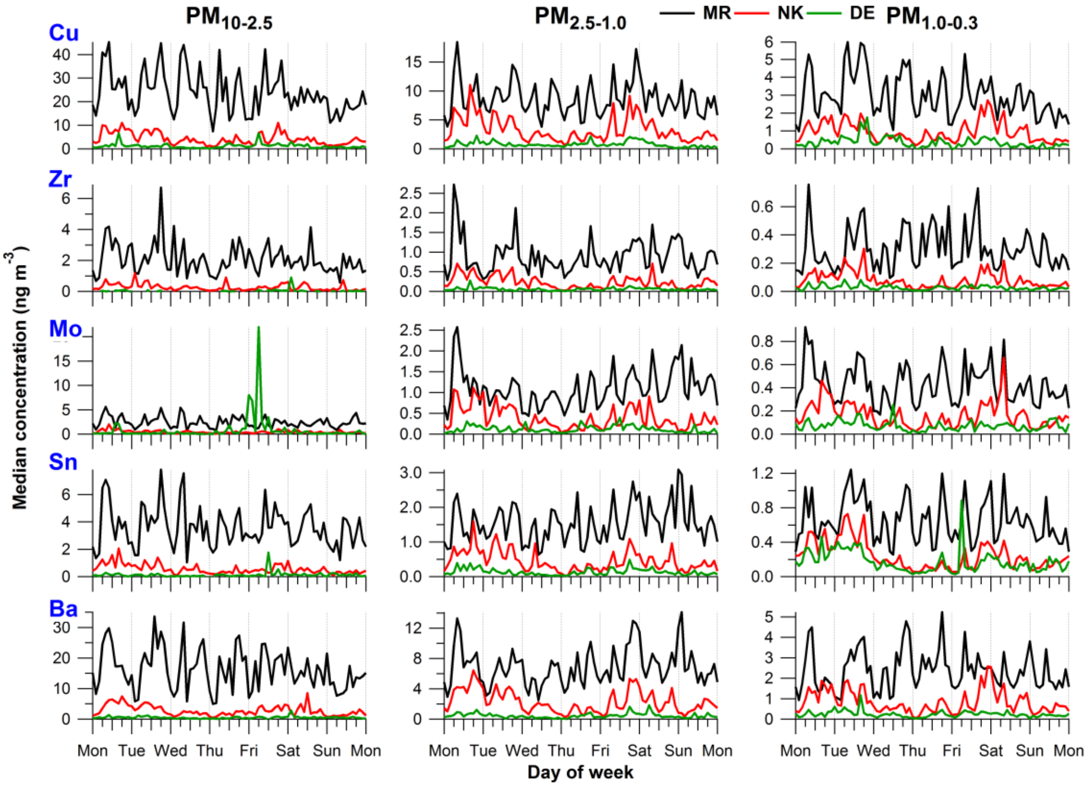

Figure S9. Continued.

References

Bearden, J. A.: X-ray wavelengths, Rev. Mod. Phys., 39, 78-124, doi:10.1103/revmodphys.39.78, 1967.

Bukowiecki, N., Hill, M., Gehrig, R., Zwicky, C. N., Lienemann, P., Hegedus, F., Falkenberg, G., Weingartner, E., and Baltensperger, U.: Trace metals in ambient air: Hourly size-segregated mass concentrations determined by synchrotron-XRF, Environ. Sci. Technol., 39, 5754-5762, 2005.

Bukowiecki, N., Lienemann, P., Zwicky, C. N., Furger, M., Richard, A., Falkenberg, G., Rickers, K., Grolimund, D., Borca, C., Hill, M., Gehrig, R., and Baltensperger, U.: X-ray fluorescence spectrometry for high throughput analysis of atmospheric aerosol samples: The benefits of synchrotron X-rays, Spectrochim. Acta B, 63, 929-938, 2008.

Bukowiecki, N., Richard, A., Furger, M., Weingartner, E., Aguirre, M., Huthwelker, T., Lienemann, P., Gehrig, R., and Baltensperger, U.: Deposition uniformity and particle size distribution of ambient aerosol collected with a rotating drum impactor, Aerosol Sci. Technol., 43, 891-901, 2009.

DeCarlo, P. F., Slowik, J. G., Worsnop, D. R., Davidovits, P., and Jimenez, J. L.: Particle morphology and density characterization by combined mobility and aerodynamic diameter measurements. Part 1: Theory, Aerosol Sci. Technol., 38, 1185-1205, doi:10.1080/027868290903907, 2004.

Richard, A., Bukowiecki, N., Lienemann, P., Furger, M., Fierz, M., Minguillon, M. C., Weideli, B., Figi, R., Flechsig, U., Appel, K., Prevot, A. S. H., and Baltensperger, U.: Quantitative sampling and analysis of trace elements in atmospheric aerosols: impactor characterization and synchrotron-XRF mass calibration, Atmos. Meas. Tech., 3, 1473-1485, 2010.

Sole, V. A., Papillon, E., Cotte, M., Walter, P., and Susini, J.: A multiplatform code for the analysis of energy-dispersive X-ray fluorescence spectra, Spectrochim. Acta B, 62, 63-68, 2007.

Van Espen, P., Janssens, K., and Nobels, J.: AXIL-PC, software for the analysis of complex X-ray spectra, Chemometrics Intell. Lab. Syst., 1, 109-114, 1986.